



# A platform for high performance photon correlation measurements

Iman Esmaeil Zadeh,<sup>\*,†,‡</sup> Johannes W. N. Los <sup>\*,‡</sup>, Ronan B. M. Gourgues,<sup>‡</sup> Jin Chang,<sup>¶</sup> Ali W. Elshaari,<sup>§</sup> Julien Zichi,<sup>§</sup> Yuri J. van Staaden,<sup>¶</sup> Jeroen Swens,<sup>¶</sup> Nima Kalhor,<sup>‡</sup> Antonio Guardiani,<sup>‡</sup> Yun Meng,<sup>||,⊥</sup> Kai Zou,<sup>||,⊥</sup> Sergiy Dobrovolskiy,<sup>‡</sup> Andreas W. Fognini,<sup>‡</sup> Dennis R. Schaart,<sup>#</sup> Dan Dalacu,<sup>@</sup> Philip J. Poole,<sup>@</sup> Michael E. Reimer,<sup>△</sup> Xiaolong Hu,<sup>||,⊥</sup> Sylvania F. Pereira,<sup>¶</sup> Val Zwiller,<sup>§,‡</sup> and Sander N. Dorenbos<sup>‡</sup>

<sup>†</sup>*Optics Research Group, ImPhys Department, Faculty of Applied Sciences, Delft University of Technology, Delft 2628 CJ, The Netherlands.*

<sup>‡</sup>*Single Quantum B.V., Delft 2628 CJ, The Netherlands.*

<sup>¶</sup>*Optics Research Group, ImPhys Department, Faculty of Applied Sciences, Delft University of Technology, Delft 2628 CJ, The Netherlands.*

<sup>§</sup>*Quantum Nano Photonics Group, Department of Applied Physics, Royal Institute of Technology (KTH), Stockholm 106 91, Sweden*

<sup>||</sup>*School of Precision Instrument and Optoelectronic Engineering, Tianjin University, Tianjin 300072, China.*

<sup>⊥</sup>*Key Laboratory of Optoelectronic Information Science and Technology, Ministry of Education, Tianjin 300072, China.*

<sup>#</sup>*Medical Physics & Technology, Radiation Science & Technology department, Faculty of Applied Sciences, Delft University of Technology*

<sup>@</sup>*National Research Council of Canada, Ottawa, ON K1A 0R6, Canada.*

<sup>△</sup>*Institute for Quantum Computing and Department of Electrical & Computer Engineering, University of Waterloo, Waterloo, ON N2L 3G1, Canada.*

E-mail: i.esmaeilzadeh@tudelft.nl

---

\* These authors contributed to this work equally

## Abstract

A broad range of scientific and industrial disciplines require precise optical measurements at very low light levels. Single-photon detectors combining high efficiency and high time resolution are pivotal in such experiments. By using relatively thick films of NbTiN (8-11 nm) and improving the pattern fidelity of the nano-structure of the superconducting nanowire single-photon detectors (SNSPD), we fabricated devices demonstrating superior performance over all previously reported detectors in the combination of efficiency and time resolution. Our findings prove that small variations in the nanowire width, in the order of a few nanometers, can lead to a significant penalty on their temporal response. Addressing these issues, we consistently achieved high time resolution (best device 7.7 ps, other devices  $\sim 10$ -16 ps) simultaneously with high system detection efficiencies (80 – 90%) in the wavelength range of 780-1000 nm, as well as in the telecom bands (1310-1550 nm). The use of thicker films allowed us to fabricate large-area multi-pixel devices with homogeneous pixel performance. We first fabricated and characterized a  $100 \times 100 \mu m^2$  16-pixel detector and showed there was little variation among individual pixels. Additionally, to showcase the power of our platform, we fabricated and characterized 4-pixel multimode fiber-coupled detectors and carried out photon correlation experiments on a nanowire quantum dot resulting in  $g^2(0)$  values lower than 0.04. The multi-pixel detectors alleviate the need for beamsplitters and can be used for higher order correlations with promising prospects not only in the field of quantum optics, but also in bio-imaging applications, such as fluorescence microscopy and positron emission tomography.

## Introduction

SNSPDs have already pushed the limits in several fields such as CMOS testing,<sup>1</sup> biomedical imaging,<sup>2</sup> laser ranging,<sup>3</sup> and quantum communication.<sup>4,5</sup> These detectors have unparalleled performance: high efficiency ( $>90\%$ ),<sup>6-8</sup> time resolution ( $<15$  ps),<sup>8,9</sup> and count-rate.<sup>10</sup> Yet, for studying fast phenomena in chemistry, biology, physics, detectors with better timing

jitter are required. Although direct high time-resolution measurements are possible, for example with streak cameras, they suffer from low detection efficiencies typically  $< 10\%$  and high dark count rates,<sup>11,12</sup> moreover they are bulky and costly. Meanwhile, the fiber coupled SNSPDs allow for a cost efficient integration of many high performance detectors in a single cryostat. Here we demonstrate SNSPDs made of relatively thick NbTiN films with superior time resolution and high efficiencies. Moreover, we show large area sensors using arrays of SNSPDs with minimal variation in performance over the array. In addition to optical imaging applications, this technology could be used to read-out fast scintillators, potentially enabling the detection of ionizing radiation with unprecedented time resolution, which is of great interest for time-of-flight positron emission tomography.<sup>13</sup> We showcase our platform by carrying out photon correlation measurements using a multi-pixel multimode fiber-coupled detector.

We fabricate our detectors from sputtered NbTiN films on top of a  $\text{SiO}_2/\text{Au}$  cavity or a distributed Bragg reflector. To achieve the highest possible absorption in the superconducting layer, increasing the critical current and reducing kinetic inductance (and hence the deadtime), thicker films are desirable.<sup>8</sup> On the other hand, increasing the film thickness leads to a higher energy gap and reduction of the kinetic energy of the quasiparticles. Therefore, for such films, it is challenging to reach saturation of the internal efficiency, and hence, both the material properties of the film and the fabrication uniformity of the SNSPD nanowire meander have to be controlled.

## Fabrication and Characterization

Magnetron sputtering was used to deposit the films and similar to ref.<sup>14</sup>, we varied the sputtering parameters to achieve both high current and saturation of internal efficiency at the wavelength of 820 nm (we also optimized films and fabricated high performance devices optimized for the telecom wavelength range, see supporting information). Figure1(a) represents,

similar to ref.<sup>14</sup>, the measured internal efficiency (the saturation plateau,  $\frac{I_c - I_{sat}}{I_c}$ ) for detectors made from films with different partial Nb contents. As it can be observed, all detectors with different Nb fractions show a saturation plateau, therefore, to enhance the signal to noise ratio and hence the timing jitter, we based our choice on the films which provided the highest critical current density and highest sheet resistance. All devices, unless mentioned, are fabricated from films with a Nb partial ratio of 0.85 ( $\text{Nb}_{0.85}\text{Ti}_{0.15}\text{N}$ ). This composition yields detectors which not only have a high critical current density and a long saturation plateau (at the studied wavelength), but also can be operated at higher temperatures<sup>15</sup> and are compatible with large scale integrated nanophotonics.<sup>16</sup> We optimized our fabrication recipe and fabricated detectors with high uniformity. High resolution SEM images of sample devices are shown in Figure1(b).

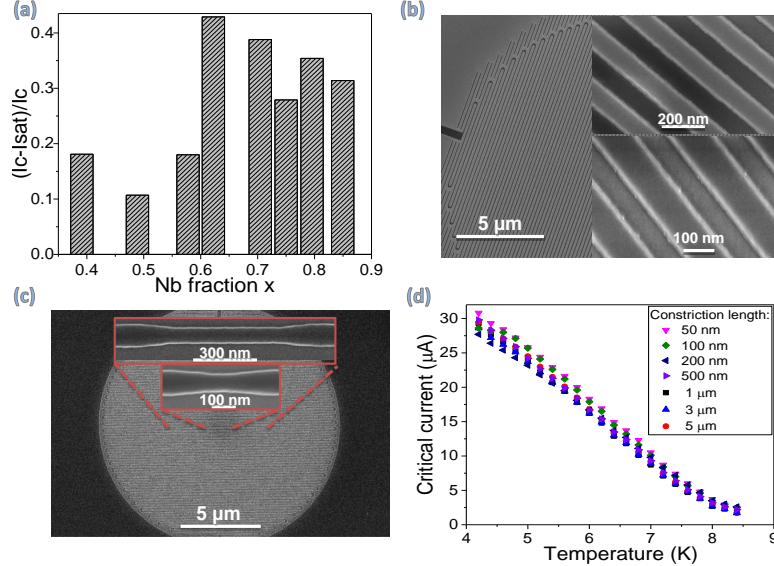


Figure 1: (a) Saturation of internal efficiency for sputtered films of  $\text{Nb}_x\text{Ti}(1-x)\text{N}$  versus their Nb fraction at 830 nm. (b) SEM images of devices fabricated and optimized for the wavelength range of 800-900 nm. Top and bottom insets show devices with filling factor of  $\sim 0.55$  and  $0.6$ , respectively. (c) Meander with a short constricted region. The main nanowire has a width of 100 nm and the width in the constriction region is 70 nm. The constriction length varies from 50 nm to 5000 nm and is always a straight section (not including bends). (d) Critical currents of devices described in (c) versus temperature. No significant change of critical currents was observed when changing the constriction length.

Localized inhomogeneities are known to limit the critical current of SNSPDs made out of

thin crystalline films (such as NbN and NbTiN).<sup>17</sup> We investigate whether the inhomogeneities can also affect our thicker NbTiN films by embedding short constrictions in the meandering detector as shown in Figure 1(c). The main SNSPD meander had a width of 100 nm and the constriction was 70 nm wide. The length of this constriction was varied from 50 nm to 5  $\mu$ m (always a straight section wire with no bends) and we measured their critical currents at several temperatures in the range of 4.2 K to 8.5 K (Figure 1(d)). We did not observe any significant degradation of critical current with the increase of constriction length. Furthermore, many of our fabricated shorter SNSPDs ( $\sim 400 \mu$ m long) and longer SNSPDs ( $\sim 4$  mm long) showed similar critical currents.

It has been shown that local variation of nanowire width can influence the time resolution of SNSPDs.<sup>18</sup> To investigate the relevance of these local variations on the time resolution of our devices, we fabricate and characterize SNSPDs sectioned in two regions with different nanowire widths. Figure 2(a) is an illustration of such a two sectioned SNSPD and Figure 2(b) shows an SEM image of a fabricated device with 70 nm and 77 nm wide sections. We designed the device so that the length of 77 nm wide section is about  $\sim 7.7$  times longer than the 70 nm wide section. We measure the SNSPD jitter by correlating the SNSPD pulses (start signal) with that of a pulsed laser (1060 nm, 5.08 ps, 48.6 MHz) as stop signal, shown in Figure 2(c). Two distinct peaks can be observed, corresponding to the two different meander sections. We ascribe the peak on the right side to the 70 nm wide section because of its higher resistance which leads to faster risetime and hence earlier start signal. The fast risetime also leads to a narrower distribution since noise jitter is inversely proportional to the slope. The left side peak is ascribed to the 77 nm wide section which has the lower resistance and hence the late start signal. We also investigated the temporal profile of detection events as a function of bias current, as shown in Figure 2(d).

To better understand the bias-current-dependent histograms of our two-section device, we numerically simulated these histograms including electronic-noise-induced timing jitter,<sup>19,20</sup> geometric timing jitter,<sup>21</sup> and inhomogeneity-induced timing jitter,<sup>22</sup> see supporting infor-

mation for details. As presented in Figure 2(e), the simulated histograms show the features of double peaks which were also observed experimentally (Figure 2(d)). The system detection efficiency of each section determines the area under each peak, and therefore, is the major factor affecting the amplitude of each. The separation between the two peaks is the difference of time delays. We see that the simulated separations between the two peaks are larger than the measured results; so that at low bias level, two distinct peaks are obtained in simulation, as opposed to a main peak with a shoulder as observed experimentally. This discrepancy is mainly due to the fact that simulated leading edges of these time-domain pulses do not perfectly match the experimental results (see supporting information).

Nanofabrication of SNSPDs can introduce imperfections; the nanowire width may vary along the meander for a number of systemic and fabrication issues. A common factor is the proximity effect during electron beam lithography. The proximity effect can cause center areas of the detector to have a wider or narrower width (depending on the tone, thickness and chemistry of the ebeam resist as well as the properties of the substrate, see supporting information for examples of proximity effect simulations), resulting in a similar behaviour to that of Figure 2(c). However, due to the limitations of the experimental setups, it is not always possible to resolve the peaks, yet we observed two distinct peaks in the temporal response of devices with a width difference as low as 2 nm (supporting information). It should be noted that if the device has more gradual widths variations (which is plausible considering the profile of proximity effects), instead of distinct peaks, one would expect a single broad peak. Proximity effects can be accounted and compensated for, however, it requires simulation, optimization and verification for each single pattern, resist, and every electron beam lithography system. As our simulation suggests (supporting information) and from the literature,<sup>23</sup> that it is possible to significantly reduce the PE using thinner ebeam resists. We tuned the resist thickness (for negative tone, 25-30 nm XR1541, and for positive tone 90-100 nm PMMA/AR-P 6200.04), the reactive ion etching chemistry (12.5 sccm  $SF_6$ , 3.4 sccm  $O_2$ , and a process pressure of  $\sim 4\mu bar$ ), and etching power and time (50 W and

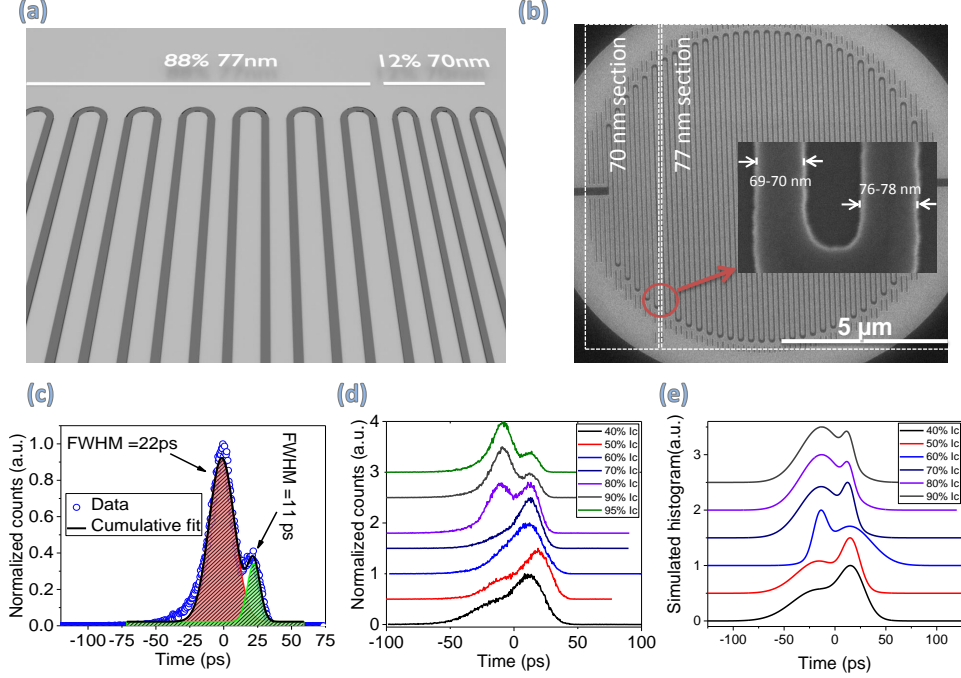


Figure 2: (a) Schematic illustration of a two section SNSPD: having  $\sim 12\%$  (of its area) 70 nm nanowire width and  $\sim 88\%$  a width of 77 nm. (b) SEM image of a two section SNSPD. The inset shows a magnified high resolution SEM of the transition between 70 and 77 nm. The measured values were in good agreement with the design (also see supporting information for more SEM images). (c) Time jitter for the two-section SNSPD, at a bias current equivalent to 95% of critical current. Two distinct peaks can be observed, which correspond to the two different meander sections. (d) Time jitter measurements for the same detector at various bias currents. It can be observed that at lower biases the detections mostly occur in the 70 nm section (higher internal saturation) while at higher biases it is dominated by 77 nm section (larger surface area). This difference depends on the degree of saturation of each section. (e) Simulated correlation histograms at different bias currents.

45 seconds), and fabricated 70-100 nm wide nanowires made out of 10-13 nm thick films. The resulting detectors showed saturated internal efficiency in the wavelength range of 400-1064 nm. Note that the top section of the film has 0.5-1.5 nm oxidized layer,<sup>24</sup> preventing it from further oxidation. For high efficiency and high time resolution telecom detectors we used slightly thinner films (8.5-9.5 nm). For all fiber-coupled devices, unless otherwise clearly stated, the nanowire width and filling factor were 70 nm and 0.5, respectively.

For the measurement of high performance detectors, we packaged and characterized the detectors in a standard setup similar to.<sup>8</sup> For efficiency measurements, at each wavelength



we adjusted the input power to 10 nW and then attenuated it by 50 dB, setting an input photon flux in the range of 200-800 KCounts/second for visible to telecom wavelength range. For jitter measurements at low photon fluxes, we used a pico-second pulsed laser (same laser as was used for characterization of two-section detectors), and we kept the detector count-rate in the range of 60-100 KCount/second. Figure 3(a) and 3(b) present the efficiency and jitter measurement results for a detector optimized for the wavelength range of 880-950 nm, respectively. For other wavelengths we achieved similar performance, see supporting information. We measured a system detection efficiency of  $> 85(\pm 5\%)$  and system time resolution of  $9.23 \pm 0.05$  ps (deconvoluted 7.70 ps, see supporting information). Other devices for this wavelength had SDE of 82-91.5% and time resolution of 9.5-15 ps (see supporting information). The inset in Figure 3(b) is a logarithmic plot of the data and fit. On the left side of the jitter measurement data, a small asymmetry and deviation from the fit is observed. Besides originating from the nanowire width variation, this asymmetry could also be due to detection in the nanowire bends as reported in.<sup>25</sup> However, in comparison with<sup>25</sup> our degree of asymmetry is smaller, which most likely is explained by the non uniform illumination of our device caused by the fact that the fiber coupled detector has a diameter larger than the mode field diameter of the optical fiber. As a result, the meander bends are not efficiently illuminated. The asymmetry was stronger when we flood illuminated the detectors in a free-space setup (in this case, bends were illuminated). To achieve the best time resolution, we triggered the correlator on the steepest part of the pulses rising edge. We also studied the effect of trigger level (varying it from 10% to 80% ) on the value of the FWHM of detector jitter (see supporting information). An increase in the FWHM jitter can be observed, from 15.5 ps to 22.5 ps for a sample detector. This is likely to be caused by reduced signal to noise ratio (slower rise time or higher noise level).

We also investigated the count-rate dependence of the jitter (see supporting information). We observed that at low count-rates (below  $0.1 \times$  laser repetition-rate), the SNSPD time jitter exhibits a typical single Gaussian distribution. However, as the count-rate increases,

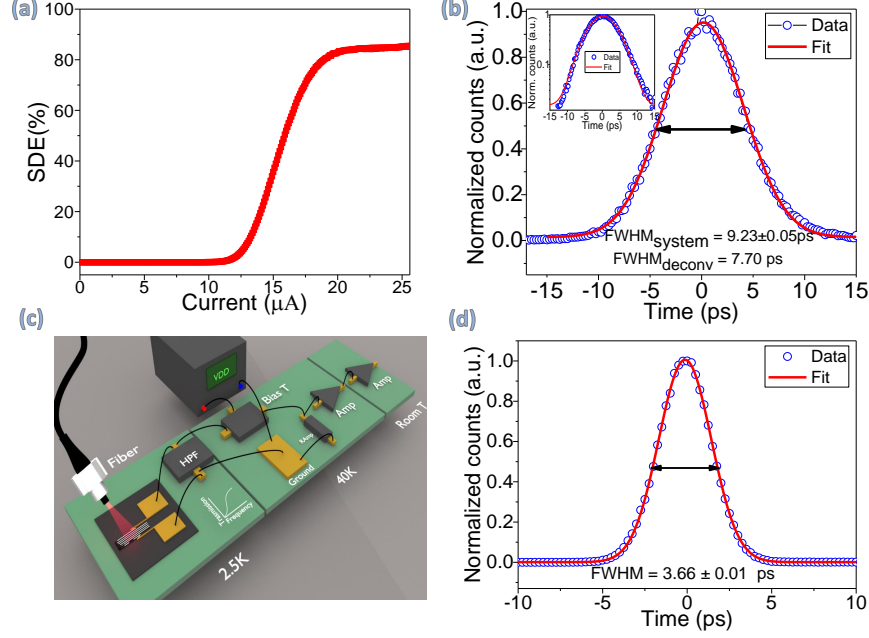


Figure 3: (a) Efficiency vs bias current for a detector at 915 nm, the peak efficiency is  $85 \pm 4.5\%$  (b) Jitter measurement for the same detector as part (a), the FWHM of the jitter, obtained from a Gaussian fit, is  $9.23 \pm 0.05$  ps. Considering the duration of the laser pulses (5.08 ps) and neglecting the contribution from the correlator and photodiode ( $\sim 2.5$  ps), we obtain an SNSPD instrument response function of 7.70 ps (see supporting information). (c) An illustration of the SNSPD readout circuit used for high photon fluxes. (d) At higher photon fluxes using our new readout circuit, from the fit to the data we calculated a system time resolution of  $3.66 \pm 0.01$  ps

other peaks start to appear in the distribution. The observation of these peaks can be explained by the fact that when the bias recovery time of a SNSPD is longer than  $\frac{1}{\text{laser rep. rate}}$ , subsequent detection events take place with an under-biased detector while detection events which are temporally further away would experience normal detection (similar to low count-rate regime). Therefore, these different cases result in different risetime/signal levels, which consequently lead to multiple peaks in the jitter measurement.

Normally, SNSPDs under high excitation powers latch into the normal mode (they become normal with no recovery to the superconducting mode). By providing a low frequency path for the SNSPD current to ground, it is possible to operate detectors at higher powers. Moreover, by using high-bandwidth low-loss coax cables, a low jitter can be achieved. We use a high pass filter, as shown in Figure 3(c), in series with the detector to allow for high

power operation together with low jitter. The low-pass filter made it possible to operate the detector with higher powers (1-10 nW). With higher intensity, we make sure that every single laser pulse is filled with several photons. Therefore, the risetime and signal level stays constant for all detection events and the temporal distance between photons become shorter. Moreover, at these high powers, any SNSPD intrinsic/geometry contribution to the jitter is negligible as only the fastest events trigger the correlator. To this end the only limit we observed was the electrical noise and limited bandwidth of the amplifiers. The result of time jitter measurement with multi-photon excitation ( $>100$  photons per pulse) is shown in Figure 3(d), demonstrating a very high time-resolution of 3.66 ps ( $<3$  ps after decoupling the contributions from the correlator and the photodiode, see supplementary).

## Quantum Correlation with a Multi-Pixel SNSPD

Many optical experiments in chemistry, biology and material science deal with scattered light which cannot be efficiently collected and coupled into single mode optical fibers. Therefore, sensors with large active areas are required. SNSPDs with large active areas have gained attention in the recent years and several works on single pixel<sup>26–29</sup> and multi-pixel devices<sup>30–32</sup> have been reported. Compared to Multi-pixel devices, Single-pixel large-area devices are less complex and require only one readout channel. However there is a price to pay, since many performance parameters of SNSPDs such as deadtime and jitter and also fabrication yield suffer as the device length is increased. Until now these factors have limited the work of extending the size of single-pixel SNSPDs.

For multi-pixel SNSPD arrays, as the operation point and performance of individual pixels are usually not uniform, scaling these sensors also pose practical implementation challenges. Here we demonstrate, using our thick NbTiN films, multi-pixel arrays with small variations in performance of the pixels. Figure 4(a) show SEM images of a fabricated 16 pixel SNSPD array covering an area of  $100 \times 100 \mu m^2$  (pixel size  $25 \times 25 \mu m^2$ ). We measure

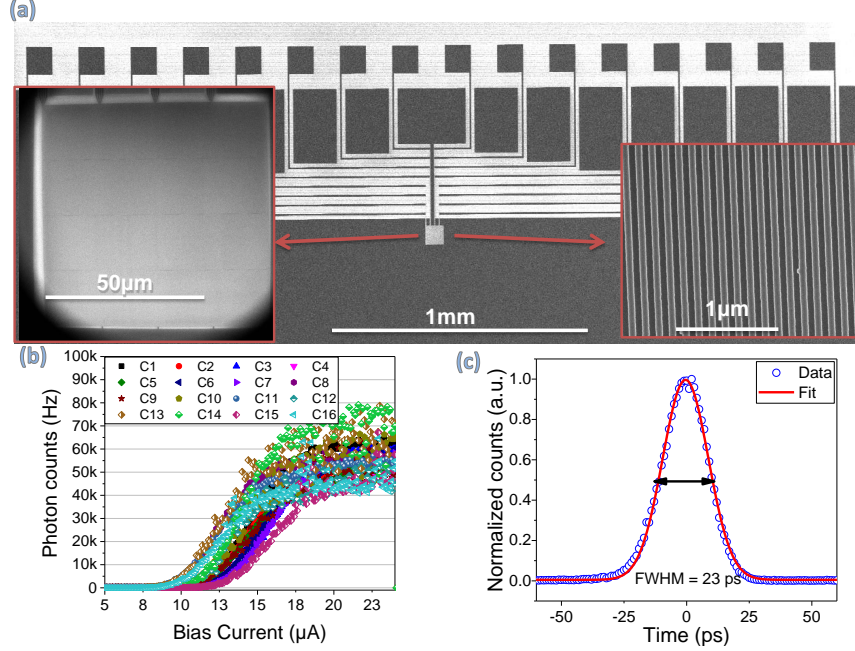


Figure 4: (a) SEM image of a fabricated 16 pixel SNSPD array covering an area of  $100 \times 100 \mu\text{m}^2$  (pixel size  $25 \times 25 \mu\text{m}^2$ ). The two insets show magnified images of the sensor array. (b) Photon count rate versus bias current for different pixels of the SNSPD array. The performance of different pixels are similar and we attribute the small differences in pixels responses to the fact that the data was collected in two cooldown cycles (temperature and illumination variation). Nevertheless, for a bias current  $>20 \mu\text{A}$ , all pixels reach saturation of internal efficiency. (c) Timing jitter measurement for one of the pixels. The measured system jitter of 23 ps is  $>25$  times better if we only consider the reported geometrical jitter in other platforms.

the photon count rate versus bias current for different pixels of the SNSPD array using a flood-illumination setup at 670 nm. The results are presented in Figure 4(b). It can be observed that the performance of all pixels are similar (for a bias current  $>20 \mu\text{A}$ , all pixels reach saturation of internal efficiency) and therefore, a much simpler biasing circuit can be used. We attribute the small differences in pixels responses to the fact that the data was collected in two cooldown cycles (cooldown 1: pixels 1-8, cooldown 2: pixels 9-16) and the temperature and illumination might had small variations (also within one cooldown there might be small variations in uniformity of illumination, see supporting information). We also measured the time jitter for some pixels of the array, the results of one such measurement is provided in Figure 4(c). The measured system jitter of 23 ps for a  $\sim 4.46$  mm long detector

is  $>25$  times better than other platforms<sup>33–35</sup> even considering only the geometrical jitter, which indicates that the electromagnetic field does not have as high confinement in our platform as detectors made from thinner films (capacitive coupling of signal between the lines).

The multi-element detectors are of particular interest in quantum optics as they provide direct photon correlation measurements with no need of spatially splitting the beam to different detectors. We carry out antibunching measurements using a 4-pixel multimode fiber coupled SNSPD on a semiconductor nanowire quantum dot. These sources have been extensively studied in the literature and have demonstrated promising performance in terms of clean emission spectra,<sup>36</sup> as entangled photon sources<sup>37</sup> and for near-unity coupling to fibers.<sup>38</sup> We use a 4-pixel multimode fiber coupled SNSPD to carry photon correlation measurements on the single-photons generated by a nanowire quantum dot. SEM image of the detector is shown in Figure 4(a) with the ground pads (G), signal pads (S), and pixel labels (1, 2, 3, 4) highlighted in the figure. Our measurement setup is illustrated in Figure 4(b), a cryogenically cooled source is excited using a CW laser (516 nm) and collected photons are filtered using a monochromator (Princeton Instrument Acton 2750) and are coupled to the detector through a graded index 50  $\mu m$  fiber. We conduct photon correlation measurements between different pixel pairs of the detector, and the results for 3 of these pairs are presented in Figure 4(c) (unprocessed data are available in the supporting information). The measured low value of  $g^2(0)$ , consistent or better than previously measured  $g^2(0)$  on similar sources,<sup>39</sup> without using any beamsplitter demonstrates the usefulness and versatility of such detectors.

## Conclusion

We demonstrated superconducting nanowire single-photon detectors (SNSPD), fabricated from NbTiN thick films, combining high time resolution and high efficiencies at the same

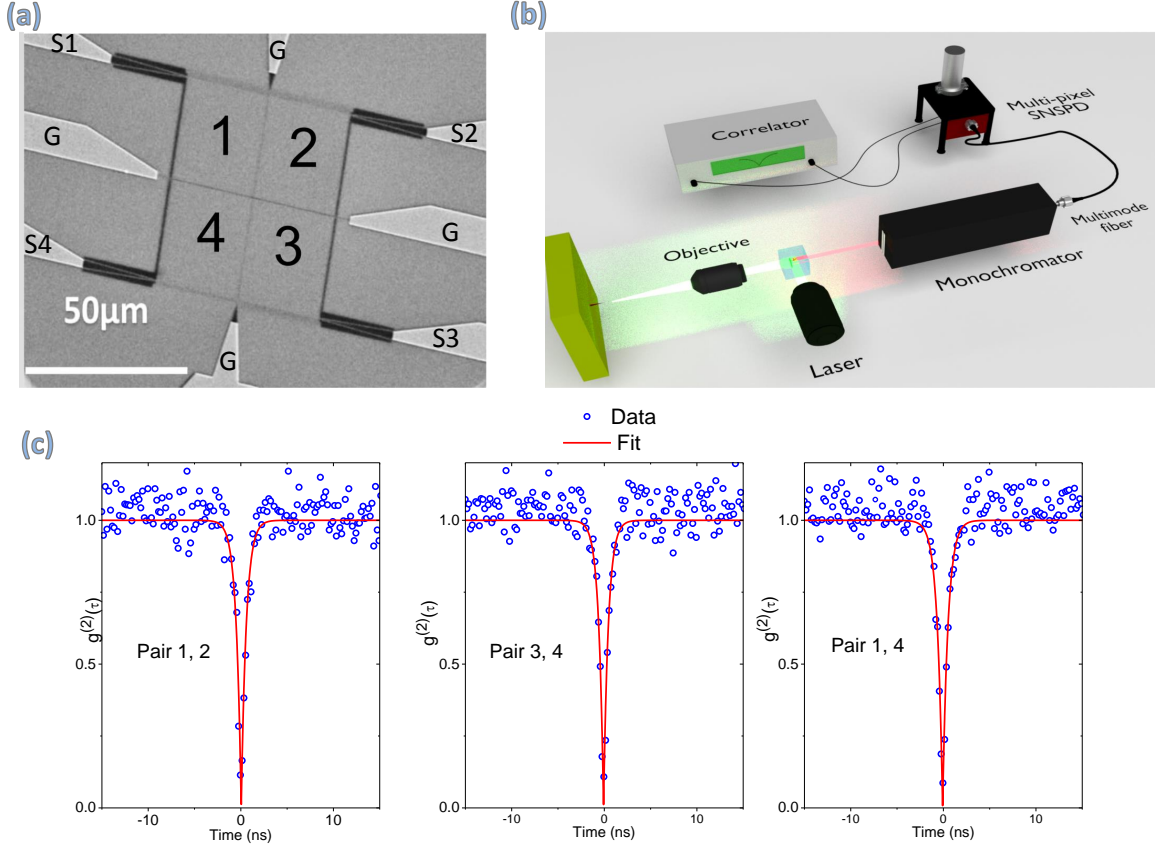


Figure 5: (a) SEM image of a fiber-coupled 4-pixel device covering an area of  $50 \times 50 \mu\text{m}^2$ . (b) Illustration of the photon antibunching measurement setup used to benchmark the 4-pixel detector. (c) Results of photon correlation measurements with three out of six possible pixel pair combinations (complete dataset can be found in supporting information). All pair combinations yield similar outcomes (depending on binning: a  $g^2(0)$  between 0.03 and 0.1) while the fit at time 0 vanishes completely. The difference between the data and the fit is mainly due to timing jitter induced by a path-length difference in the monochromator (see supporting information).

time. The influence of fabrication imperfections on the time resolution of SNSPDs was studied and it was revealed that a small variation in the order of a few nanometer can significantly influence the timing jitter. We showed that thicker films of NbTiN are less susceptible to small local material imperfections and therefore, a good candidate to serve as large active area high performance photonic sensors. A multi-pixel detector was showcased as a quantum correlator in a Hanbury Brown and Twiss experiment without using a beamsplitter. The resulting low  $g^2(0)$  demonstrates the potential of such devices not only in the field of quantum

optics, but also in the fields such as fluorescence microscopy. Large-area multi-pixel SNSPDs are furthermore expected to have bright prospects in ultra-fast optical and medical imaging applications.

## Acknowledgement

I. E. Z., A. W. E., V. Z., D. R. S., and Single Quantum B.v. acknowledge the supports from the ATTRACT project funded by the EC under Grant Agreement 777222. I. E. Z. acknowledges the support of Nederlandse Organisatie voor Wetenschappelijk Onderzoek (NWO), LIFT-HTSM (project 680-91-202). R. B. M. G acknowledges support by the European Commission via the Marie-Sklodowska Curie action Phonsi (H2020-MSCA-ITN-642656). A. W. E. acknowledges support from the Swedish Research Council (Vetenskapsrådet) Starting Grant (ref: 2016-03905). V. Z. acknowledges funding from the Knut and Alice Wallenberg Foundation Grant "Quantum Sensors", and support from the Swedish Research Council (VR) through the VR Grant for International Recruitment of Leading Researchers (Ref 2013-7152) and Research Environment Grant (Ref 2016-06122). Y. M., K. Z., and X. H. acknowledge the support from Natural Science Foundation of Tianjin City (19JCYBJC16900).

## Supporting Information Available

The supporting information includes additional examples of high performance devices (S1), supplementary information and simulations for detectors' time jitter (S2) as well as further data on multi-pixel devices(S3).

## References

- (1) Zhang, J. et al. Noninvasive CMOS circuit testing with NbN superconducting single-photon detectors. *Electronics Letters* **2003**, *39*, 1086–1088.

- (2) Pe'er, A.; Bromberg, Y.; Dayan, B.; Silberberg, Y.; Friesem, A. A. Broadband sum-frequency generation as an efficient two-photon detector for optical tomography. *Opt. Express* **2007**, *15*, 8760–8769.
- (3) McCarthy, A.; Krichel, N. J.; Gemmell, N. R.; Ren, X.; Tanner, M. G.; Dorenbos, S. N.; Zwiller, V.; Hadfield, R. H.; Buller, G. S. Kilometer-range, high resolution depth imaging via 1560 nm wavelength single-photon detection. *Opt. Express* **2013**, *21*, 8904–8915.
- (4) Yin, J.; Cao, Y.; Liu, S.-B.; Pan, G.-S.; Wang, J.-H.; Yang, T.; Zhang, Z.-P.; Yang, F.-M.; Chen, Y.-A.; Peng, C.-Z.; Pan, J.-W. Experimental quasi-single-photon transmission from satellite to earth. *Opt. Express* **2013**, *21*, 20032–20040.
- (5) Vallone, G.; Dequal, D.; Tomasin, M.; Vedovato, F.; Schiavon, M.; Luceri, V.; Bianco, G.; Villoresi, P. Interference at the Single Photon Level Along Satellite-Ground Channels. *Phys. Rev. Lett.* **2016**, *116*, 253601.
- (6) Marsili, F.; Verma, V. B.; Stern, J. A.; Harrington, S.; Lita, A. E.; Gerrits, T.; Vayshenker, I.; Baek, B.; Shaw, M. D.; Mirin, R. P.; Nam, S. W. Detecting single infrared photons with 93% system efficiency. *Nat Photon* **2013**, *7*, 210–214.
- (7) Zhang, W. J.; You, L. X.; Li, H.; Huang, J.; Lv, C. L.; Zhang, L.; Liu, X. Y.; Wu, J. J.; Wang, Z.; Xie, X. M. NbN superconducting nanowire single photon detector with efficiency over 90% at 1550 nm wavelength operational at compact cryocooler temperature. *ArXiv e-prints* **2016**,
- (8) Zadeh, I. E.; Los, J. W. N.; Gourgues, R. B. M.; Steinmetz, V.; Bulgarini, G.; Dobrovolskiy, S. M.; Zwiller, V.; Dorenbos, S. N. Single-photon detectors combining high efficiency, high detection rates, and ultra-high timing resolution. *APL Photonics* **2017**, *2*, 111301.
- (9) Wu, J.; You, L.; Chen, S.; Li, H.; He, Y.; Lv, C.; Wang, Z.; Xie, X. Improving the



- timing jitter of a superconducting nanowire single-photon detection system. *Appl. Opt.* **2017**, *56*, 2195–2200.
- (10) Huang, J.; Zhang, W.; You, L.; Zhang, C.; Lv, C.; Wang, Y.; Liu, X.; Li, H.; Wang, Z. High speed superconducting nanowire single-photon detector with nine interleaved nanowires. *Superconductor Science and Technology* **2018**, *31*, 074001.
- (11) Müller, A. M.; Bardeen, C. J. Using a Streak Camera to Resolve the Motion of Molecular Excited States with Picosecond Time Resolution and 150 nm Spatial Resolution. *The Journal of Physical Chemistry C* **2007**, *111*, 12483–12489.
- (12) Hamamatsu, *Streak camera: FESCA-100 Femtosecond streak camera*, Retrieved from <https://www.hamamatsu.com/eu/en/product/photometry-systems/streak-camera/fesca-100-femtosecond-streak-camera/index.html> **2020**,
- (13) S. Seifert, H. T. v. D.; Schaart, D. R. The Lower Bound on the Timing Resolution of Photon Counting Scintillation Detectors. *Phys Med Biol.* **2012**, *57*.
- (14) Zichi, J.; Chang, J.; Steinhauer, S.; von Fieandt, K.; Los, J. W. N.; Visser, G.; Kalhor, N.; Lettner, T.; Elshaari, A. W.; Zadeh, I. E.; Zwiller, V. Optimizing the stoichiometry of ultrathin NbTiN films for high-performance superconducting nanowire single-photon detectors. *Opt. Express* **2019**, *27*, 26579–26587.
- (15) Gourgues, R.; Los, J. W. N.; Zichi, J.; Chang, J.; Kalhor, N.; Bulgarini, G.; Dorenbos, S. N.; Zwiller, V.; Zadeh, I. E. Superconducting nanowire single photon detectors operating at temperature from 4 to 7 K. *Opt. Express* **2019**, *27*, 24601–24609.
- (16) Gourgues, R.; Zadeh, I. E.; Elshaari, A. W.; Bulgarini, G.; Los, J. W. N.; Zichi, J.; Dalacu, D.; Poole, P. J.; Dorenbos, S. N.; Zwiller, V. Controlled integration of selected detectors and emitters in photonic integrated circuits. *Opt. Express* **2019**, *27*, 3710–3716.

- (17) Gaudio, R.; op 't Hoog, K. P. M.; Zhou, Z.; Sahin, D.; Fiore, A. Inhomogeneous critical current in nanowire superconducting single-photon detectors. *Applied Physics Letters* **2014**, *105*, 222602.
- (18) O'Connor, J. A.; Tanner, M. G.; Natarajan, C. M.; Buller, G. S.; Warburton, R. J.; Miki, S.; Wang, Z.; Nam, S. W.; Hadfield, R. H. Spatial dependence of output pulse delay in a niobium nitride nanowire superconducting single-photon detector. *Applied Physics Letters* **2011**, *98*, 201116.
- (19) Zhao, Q.; Zhang, L.; Jia, T.; Kang, L.; Xu, W.; Chen, J.; Wu, P. Intrinsic timing jitter of superconducting nanowire single-photon detectors. *Applied Physics B* **2011**, *104*, 673–678.
- (20) You, L.; Yang, X.; He, Y.; Zhang, W.; Liu, D.; Zhang, W.; Zhang, L.; Zhang, L.; Liu, X.; Chen, S.; Wang, Z.; Xie, X. Jitter analysis of a superconducting nanowire single photon detector. *AIP Advances* **2013**, *3*, 072135.
- (21) Calandri, N.; Zhao, Q.-Y.; Zhu, D.; Dane, A.; Berggren, K. K. Superconducting nanowire detector jitter limited by detector geometry. *Applied Physics Letters* **2016**, *109*, 152601.
- (22) Cheng, Y.; Gu, C.; Hu, X. Inhomogeneity-induced timing jitter of superconducting nanowire single-photon detectors. *Applied Physics Letters* **2017**, *111*, 062604.
- (23) Li, P. A Review of Proximity Effect Correction in Electron-beam Lithography. *ArXiv e-prints* **2015**,
- (24) Cheng, R.; Guo, X.; Ma, X.; Fan, L.; Fong, K. Y.; Poot, M.; Tang, H. X. Self-aligned multi-channel superconducting nanowire single-photon detectors. *Opt. Express* **2016**, *24*, 27070–27076.

- (25) Sidorova, M.; Semenov, A.; Hübers, H.-W.; Charaev, I.; Kuzmin, A.; Doerner, S.; Siegel, M. Physical mechanisms of timing jitter in photon detection by current-carrying superconducting nanowires. *Phys. Rev. B* **2017**, *96*, 184504.
- (26) Liu, D.; Miki, S.; Yamashita, T.; You, L.; Wang, Z.; Terai, H. Multimode fiber-coupled superconducting nanowire single-photon detector with 70% system efficiency at visible wavelength. *Opt. Express* **2014**, *22*, 21167–21174.
- (27) Li, H.; Zhang, L.; You, L.; Yang, X.; Zhang, W.; Liu, X.; Chen, S.; Wang, Z.; Xie, X. Large-sensitive-area superconducting nanowire single-photon detector at 850 nm with high detection efficiency. *Opt. Express* **2015**, *23*, 17301–17308.
- (28) Wollman, E. E.; Verma, V. B.; Beyer, A. D.; Briggs, R. M.; Korzh, B.; Allmaras, J. P.; Marsili, F.; Lita, A. E.; Mirin, R. P.; Nam, S. W.; Shaw, M. D. UV superconducting nanowire single-photon detectors with high efficiency, low noise, and 4 K operating temperature. *Opt. Express* **2017**, *25*, 26792–26801.
- (29) Chang, J.; Zadeh, I. E.; Los, J. W. N.; Zichi, J.; Fognini, A.; Gevers, M.; Dorenbos, S.; Pereira, S. F.; Urbach, P.; Zwiller, V. Multimode-fiber-coupled superconducting nanowire single-photon detectors with high detection efficiency and time resolution. *Appl. Opt.* **2019**, *58*, 9803–9807.
- (30) Allman, M. S.; Verma, V. B.; Stevens, M.; Gerrits, T.; Horansky, R. D.; Lita, A. E.; Marsili, F.; Beyer, A.; Shaw, M. D.; Kumor, D.; Mirin, R.; Nam, S. W. A near-infrared 64-pixel superconducting nanowire single photon detector array with integrated multiplexed readout. *Applied Physics Letters* **2015**, *106*, 192601.
- (31) Allmaras, J. P.; Beyer, A. D.; Briggs, R. M.; Marsili, F.; Shaw, M. D.; Resta, G. V.; Stern, J. A.; Verma, V. B.; Mirin, R. P.; Nam, S. W.; Farr, W. H. Large-Area 64-pixel Array of WSi Superconducting Nanowire Single Photon Detectors. Conference on Lasers and Electro-Optics. 2017; p JTh3E.7.

- (32) Miyajima, S.; Yabuno, M.; Miki, S.; Yamashita, T.; Terai, H. High-time-resolved 64-channel single-flux quantum-based address encoder integrated with a multi-pixel superconducting nanowire single-photon detector. *Opt. Express* **2018**, *26*, 29045–29054.
- (33) Kuzmin, A.; Doerner, S.; Sidorova, M.; Wuensch, S.; Ilin, K.; Siegel, M.; Semenov, A. Geometrical Jitter and Bolometric Regime in Photon Detection by Straight Superconducting Nanowire. *IEEE Transactions on Applied Superconductivity* **2019**, *29*, 1–5.
- (34) Santavicca, D. F.; Adams, J. K.; Grant, L. E.; McCaughan, A. N.; Berggren, K. K. Microwave dynamics of high aspect ratio superconducting nanowires studied using self-resonance. *Journal of Applied Physics* **2016**, *119*, 234302.
- (35) Zhao, Q.-Y.; Santavicca, D. F.; Zhu, D.; Noble, B.; Berggren, K. K. A distributed electrical model for superconducting nanowire single photon detectors. *Applied Physics Letters* **2018**, *113*, 082601.
- (36) Dalacu, D.; Mnaymneh, K.; Lapointe, J.; Wu, X.; Poole, P. J.; Bulgarini, G.; Zwiller, V.; Reimer, M. E. Ultraclean Emission from InAsP Quantum Dots in Defect-Free Wurtzite InP Nanowires. *Nano Letters* **2012**, *12*, 5919–5923, PMID: 23066839.
- (37) Versteegh, M. A. M.; Reimer, M. E.; Jöns, K. D.; Dalacu, D.; Poole, P. J.; Gulinatti, A.; Giudice, A.; Zwiller, V. Observation of strongly entangled photon pairs from a nanowire quantum dot. *Nature Communications* **2014**, *5*, 5298.
- (38) Bulgarini, G.; Reimer, M. E.; Bouwes Bavinck, M.; Jöns, K. D.; Dalacu, D.; Poole, P. J.; Bakkers, E. P. A. M.; Zwiller, V. Nanowire Waveguides Launching Single Photons in a Gaussian Mode for Ideal Fiber Coupling. *Nano Letters* **2014**, *14*, 4102–4106, PMID: 24926884.
- (39) Zadeh, I. E.; Elshaari, A. W.; Jöns, K. D.; Fognini, A.; Dalacu, D.; Poole, P. J.; Reimer, M. E.; Zwiller, V. Deterministic Integration of Single Photon Sources in Silicon Based Photonic Circuits. *Nano Letters* **2016**, *16*, 2289–2294.

## Supporting information for

# A platform for high performance photon correlation measurements

Iman Esmaeil Zadeh\*, Johannes W. N. Los, Ronan B. M. Gourgues, Jin Chang, Ali W. Elshaari, Julien Zichi, Yuri J. van Staaden, Jeroen Swens, Nima Kalhor, Antonio Guardiani, Yun Meng, Kai Zou, Sergiy Dobrovolskiy, Andreas W. Fognini, Dennis R. Schaart, Dan Dalacu, Philip J. Poole, Michael E. Reimer, Xiaolong Hu, Sylvania F. Pereira, Val Zwiller, Sander N. Dorenbos

\* [i.esmaeilzadeh@tudelft.nl](mailto:i.esmaeilzadeh@tudelft.nl)

## S1- High performance devices

### S1.1. Examples of high performance devices at various wavelength

Beside the detectors that are discussed in the main text, we measured other high performance devices at different wavelengths. Fig. S 1 shows examples of such detectors:

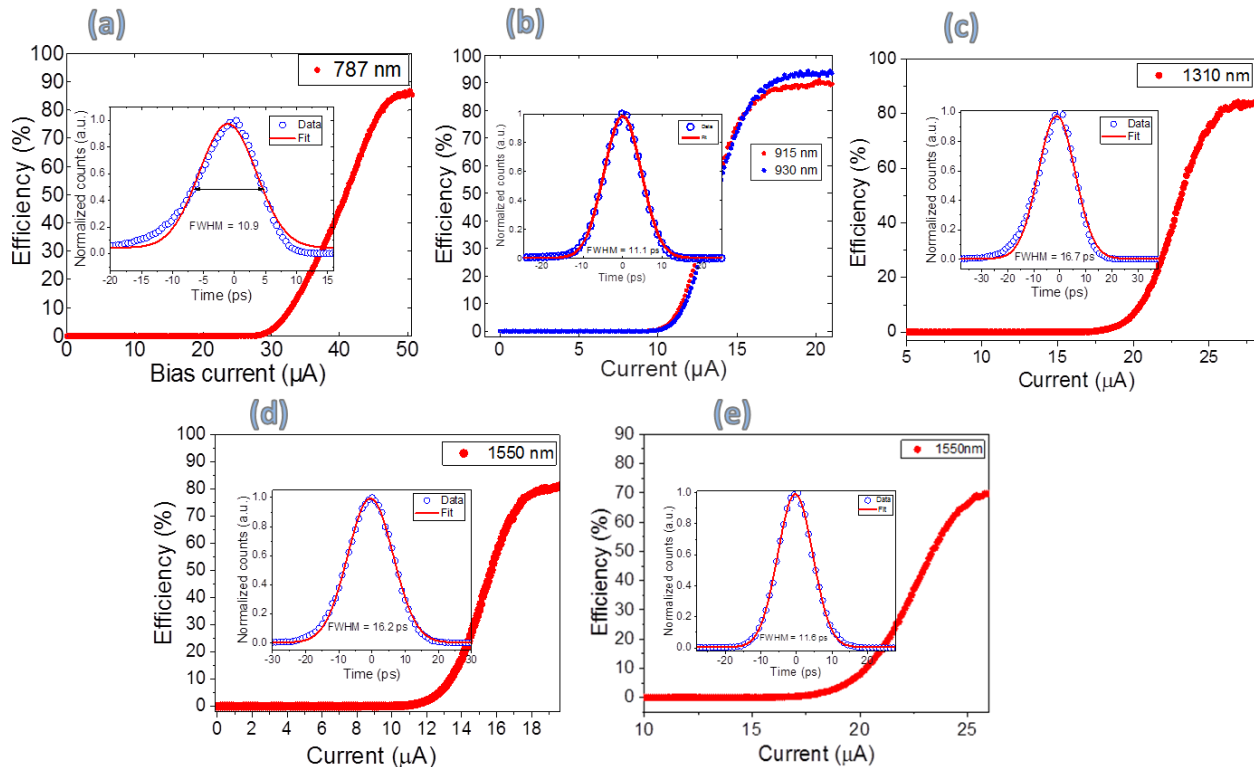


Fig. S 1 Examples of efficient single-photon detectors at various wavelength and their corresponding time resolution.

The detector that was measured at 787 nm (Fig. S 1(a)) had a nanowire linewidth of 100nm (designed), while other detectors (Fig. S 1 (b-e)) had nanowire widths of 70nm (designed) but different film thickness and compositions as discussed in the main text.

### S1.2. Performance comparison of small and big detectors

We fabricated small (diameter of 9 and 10  $\mu\text{m}$ ) and large detectors (diameter 20  $\mu\text{m}$ ) from a 11nm NbTiN film sputtered on a 4-inch wafer. The detectors were grouped together and their performance was evaluated. For the large detectors, apart from isolating broken devices (by a simple visual inspection), we selected the detectors at random.

Shown below, Fig. S 2, is the performance summary of 8 small diameter detectors (measurements at  $\lambda = 878\text{nm}$ ) and 8 randomly chosen large detectors (measured at  $\lambda = 937\text{nm}$  since the 878nm laser was damaged). The performance of the detectors are comparable: a high efficiency ( $\sim 85\%$ ) and high critical current (35-45  $\mu\text{A}$ ). The small difference in critical currents (higher for larger detectors) can be attributed to thickness gradient along the 4-inch wafer and possible nanowire width variation due to fabrication parameters such as different proximity effects for large and small detectors.

(a)

Detector#	Ic ( $\mu\text{A}$ )	Efficiency (%)	Design (widths-period- diameter)
S1	38.4	85	w70p140-10 $\mu\text{m}$
S2	39.2	88	w70p140-9 $\mu\text{m}$
S3	38.4	81	w70p140-10 $\mu\text{m}$
S4	39.5	90	w70p140-10 $\mu\text{m}$
S5	38.0	76	w70p140-10 $\mu\text{m}$
S6	36.6	85	w70p140-9 $\mu\text{m}$
S7	36	85	w70p140-9 $\mu\text{m}$
S8	39.5	82	w70p140-9 $\mu\text{m}$

(b)

Detector#	Ic( $\mu\text{A}$ )	Efficiency (%)	Design (widths-period- diameter)
B1	44.5	87	w70p140-20 $\mu\text{m}$
B2	40.9	80	w70p140-20 $\mu\text{m}$
B3	44.2	87	w70p140-20 $\mu\text{m}$
B4	43.8	90	w70p140-20 $\mu\text{m}$
B5	39.1	76	w70p140-20 $\mu\text{m}$
B6	38.2	85	w70p140-20 $\mu\text{m}$
B7	44.5	85	w70p140-20 $\mu\text{m}$
B8	45	82	w70p140-20 $\mu\text{m}$

Fig. S 2, Critical current and efficiency of (a) 8 small detectors (9 and 10 micrometers in diameter) and (b) 8 randomly chosen large detectors with a diameter of 20 $\mu\text{m}$  (length of  $\sim 4.5\text{ mm}$ ).

## S2- Jitter

### S2.1. Jitter at high count-rate

The count rate of the detector can influence its jitter. We observed that rather than only detector count rate, the ratio of the detector count rate to the laser rep-rate influences the shape of the distribution. We attenuated pulses from a 50MHz pulsed laser to get different detection rates and carried out photon correlations at each point, the results of such measurements for a detector with the parallel high-pass filter, as shown in Fig. S 3(a), are presented in Fig. S 3(b). It can be observed that at low count-rates (below  $0.1 \times$  laser repetition-rate), SNSPD time jitter exhibit a typical single Gaussian distribution. However, as the count-rate increases, other peaks appear in the distribution. The observation of these peaks can be explained by the fact that when the recovery time of the bias current of SNSPD is longer than  $\frac{1}{\text{laser rep-rate}}$ , subsequent detection events take place with an under-biased detector, while detection events which are temporally further away would experience detection with full bias current. The probability of detecting subsequent pulses (and hence the amplitude of their corresponding peak in the photon correlation distribution) depends on count-rate, being initially small and increasing as the count-rate increases. At the count rate gets close to the laser rep-rate, again the jitter starts to reduce as there is eventually only one possibility: all detection events are from subsequent pulses. By increasing the photon flux further, the latter case give us a distribution similar to the one shown in Figure 3d with 3.5 ps time jitter (main text).

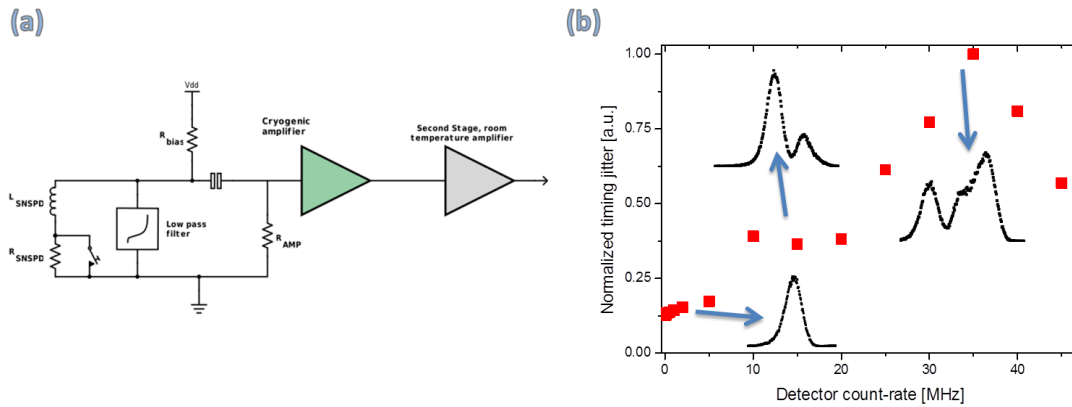


Fig. S 3, (a) A circuit schematic for the SNSPD with parallel high-pass filter (as discussed in the main text), (b) time jitter measurement versus countrate. For details see the text.

### S2.2. Contribution of laser optical pulses and the electronics on system time jitter

We have discussed about the correlation electronics used in our experiments elsewhere [1]. The electronics has a time jitter of  $\sim 2.5$ ps . However, the largest contribution to the system jitter (apart from detector itself) stems from the length of the optical pulses. To measure the contribution from the laser, we use a pulse autocorrelation setup as describe below: PulseCheck Autocorrelator was used to measure the pulse width of the Fianium WhiteLase Micro supercontinuum laser. PulseCheck Autocorrelator makes use of second-harmonic generation (SHG) to retrieve the pulse width by overlapping the laser pulse in a SHG crystal and generate a new pulse with twice the frequency of the input pulse. An interferometry scheme introduces a delay between the pulses previously split by a beam splitter and the SHG pulse energy versus delay is measured by a photomultiplier tube, as shown in Fig. S 4.

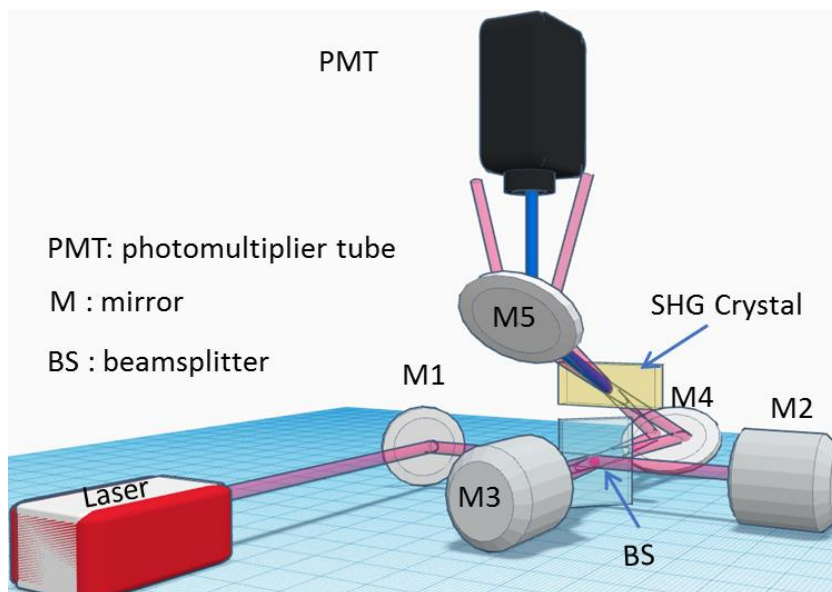


Fig. S 4, Sketch of PulseCheck Autocorrelator operated in non-collinear mode

From the Autocorrelation trace, Gaussian fitting is then performed and a Gaussian pulse width of 5.080ps is retrieved, see Fig. S 5. PulseCheck Autocorrelator was operated in non collinear mode in order to generate noise free SHG signal at the detector.

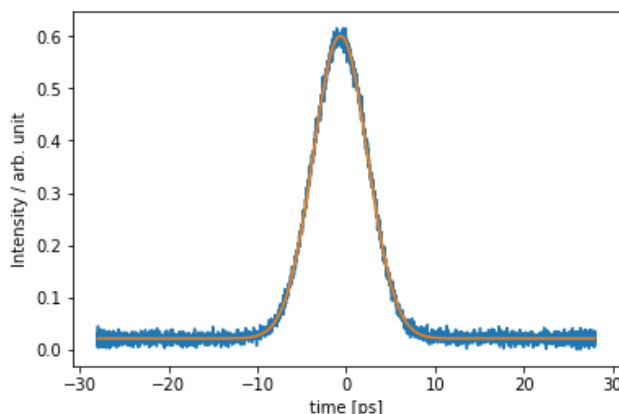


Fig. S 5, Intensity Autocorrelation of Fianium WhiteLase Micro supercontinuum laser measurement (blue) and fit (orange) yielding a 5.080ps optical pulse length.

### S2.3. Jitter versus trigger level

We measured time jitter as a function of trigger level for a detector with a minimum jitter of ~15.5ps (detector was ~500  $\mu\text{m}$  in length). The results indicate that, when the noise level is lower or the pulse has steeper slope, the time jitter is improved. The time jitter remains within 15.5-22.5ps for trigger levels in the range of 10-80%. At much lower or higher trigger levels, the jitter would suffer from low signal to noise ratio.

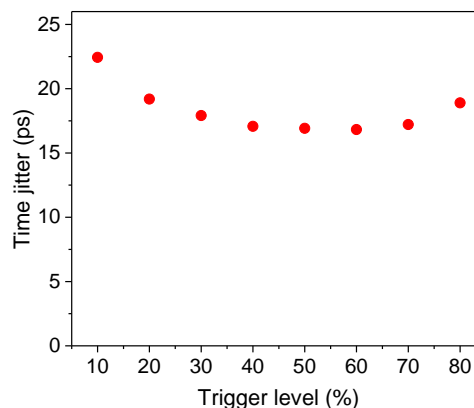


Fig. S 6, time jitter vs trigger level for detector with a minimum jitter of ~15.5 ps.



## S2.4. Jitter of two sectioned SNSPD

As described in the main text we fabricated two section detectors to study the influence of fabrication imperfections on the time jitter of SNSPDs. Below, in Fig. S 7(a) more SEM images of such an SNSPD with 70nm wide and 77nm wide sections are shown. We also fabricated detectors with 68nm wide and 70nm wide sections (only 2nm difference). Interestingly we can still observe the two peaks which we saw for the former case but in this case since the peaks are much narrower, to get a good fit, one cannot neglect the shoulder on the left side of the distribution which is possibly originated from detection in the nanowire bends, as reported in [2]. Shown in Fig. S 7 (b) is the photon correlation measurements for the two section detector with 68nm wide and 70nm wide sections at 3 different bias currents. Particularly at higher currents, where the two main peaks are narrow, the addition of third peak (as described above) is necessary to achieve a good fit.

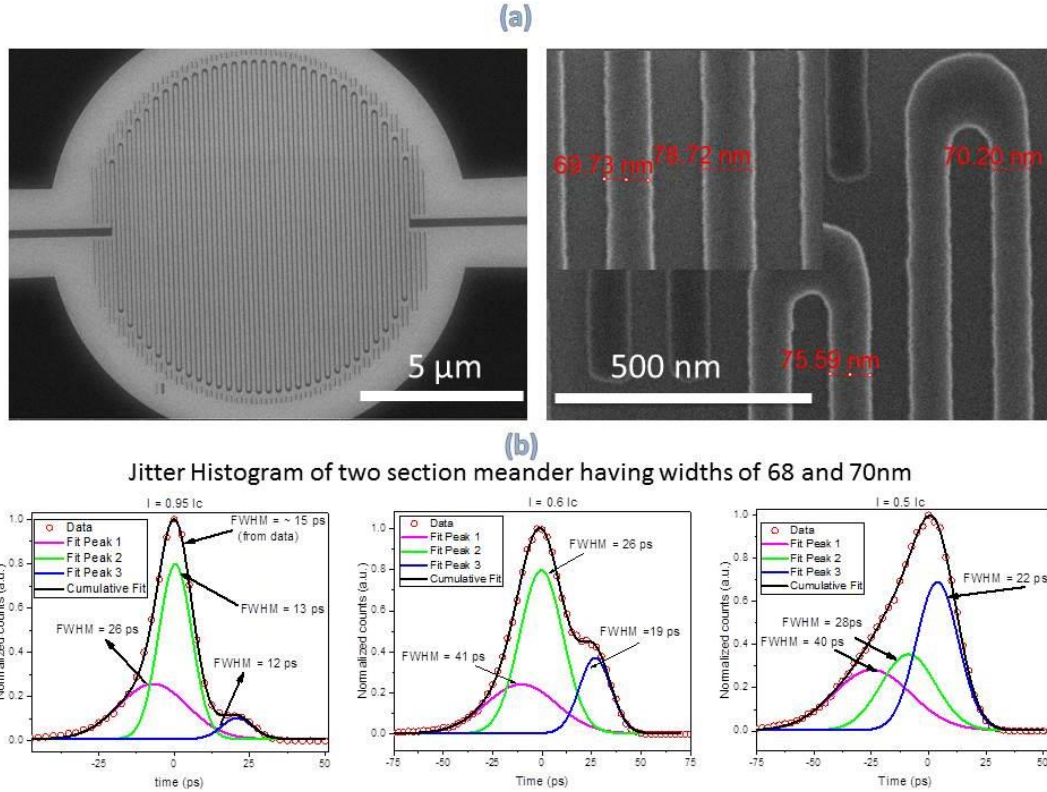


Fig. S 7, (a) More (in addition to the ones shown in the main text) SEM images of a two sectioned detector. (b) time jitter versus bias current measurements for a two section SNSPD having widths difference of only 2nm (68nm wide and 70nm wide). The two peaks attributed to the two sections are clearly visible in the time jitter measurements even for such small width difference.

## S2.5. The proximity effects

As discussed in the main text, the proximity effects can affect the linewidth of different parts of meandering nanowire. To simulate the proximity effects, we used Raith 150 e-beam lithography proximity correction software. The software provide a relative change to the ebeam dose to correct for undesired proximity effects. Fig. S 8 (a) show proximity effect corrections for a positive ebeam resist (CSAR, ARP series) with two different thicknesses and the same simulations for a negative ebeam resist (HSQ) is shown in Fig. S 8 (b) .

For ARP, the thinner resist is closer to the base dose (not much correction is required) but both cases have a good uniformity and therefore it is possible to optimize a single dose to get a

relatively uniform structure. In the case of HSQ, both thicknesses require higher doses than the base dose, however, the thinner resist presents better dose uniformity than the thicker resist (it is possible to get a relatively uniform writing by increasing the dose without correction). Note that the non-symmetric shape of the dose distribution is due to the contour that e-beam follows to expose the structure. This contour creates a non-symmetric pattern of dose distribution as well as a non-symmetric heat profile during exposure. When correctly configured, the software is capable of correcting both dose and heat distributions.

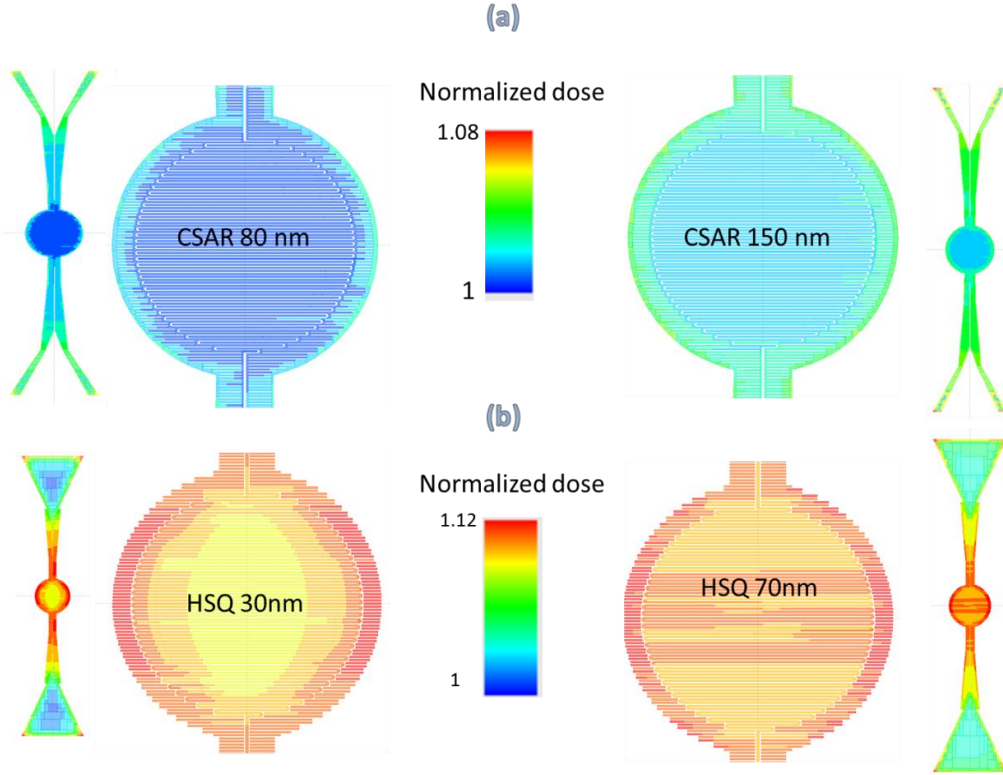


Fig. S 8, (a) Proximity effect correction for a positive ebeam resist (CSAR, ARP series) with two different thicknesses. The thinner resist is closer to the base dose (not much correction is required) but both have a good uniformity. (b) same as simulations for a negative ebeam resist (HSQ). Both thicknesses require higher doses than the base dose, however, the thinner resist presents better dose uniformity than the thicker resist (it is possible to get a relatively uniform writing by increasing the dose).

## S2.6. Simulation of jitter for two sectioned SNSPDs

As discussed in the main text, we simulated a two sectioned SNSPD by considering electronic-noise-induced timing jitter [3, 4], geometric timing jitter [5], and inhomogeneity-induced timing jitter [6]. Below is a list and the definition of parameters that are used in the simulations.

Table 1, A summary of parameters used in simulations.

Symbol	Meaning
$d$	Thickness of nanowire
$w$	Width of nanowire
$j_{c0}$	Critical current density at 0 K
$\rho_{10\text{ K}}$	Resistivity at 10 K (Not sheet resistance)
$L_k$	Kinetic inductance
$\alpha$	Thermal boundary conductivity at 10 K
$c_N$	Normal state specific heat
$c_S$	Superconducting state specific heat

$\kappa_N$	Normal state thermal conductivity
$\kappa_S$	Superconducting state thermal conductivity
$T_{\text{sub}}$	Working temperature
$T_c$	Critical temperature
$C_{\text{bt}}$	Capacitance of bias tee
$I_{\text{SW}}$	Switching current
$j_c$	Critical current density
$V$	Voltage
$\sigma_N$	Standard deviation of electric noise
$\text{TJ}_{\text{noise}}$	Noise-induced timing jitter in standard deviation
$C_g$	Capacitance between nanowire and ground
$L_g$	Inductance of nanowire
$v$	RF signal velocity along the nanowire
$\Delta t$	Transmission-line-effect-induced time delay
$\text{TJ}_{\text{geometric}}$	Transmission-line-effect-induced timing jitter in standard deviation
$\Delta$	Superconducting gap
$\bar{w}$	Mean of the distributed width
$\bar{d}$	Mean of the distributed thickness
$\bar{\Delta}$	Mean of the distributed superconducting gap
$\sigma_w$	Standard deviation of the distributed width
$\sigma_d$	Standard deviation of the distributed thickness
$\sigma_{\Delta}$	Standard deviation of the distributed superconducting gap
$l_g^w$	Granularity <sup>1</sup> of the distributed width
$l_g^d$	Granularity <sup>1</sup> of the distributed thickness
$l_g^{\Delta}$	Granularity <sup>1</sup> of the distributed superconducting gap
$a$	Gaussian fit parameter, no physical meaning
$t$	Time
$t_1$	Electro-thermal-evolution-induced time delay
$\text{TJ}_{\text{inhomogeneity}}$	Inhomogeneity-induced timing jitter in standard deviation
$t_0$	Overall time delay
$\text{TJ}_{\text{overall}}$	Overall timing jitter in standard deviation
$F$	Gaussian function
$A_0$	Gaussian fit parameter, no physical meaning
$\text{DE}$	Detection efficiency

1. The granularity is the characteristic length below which a property of the nanowire can be considered as being uniform and above which the property varies.

The total time jitter distribution can be constructed by considering all of above mentioned jitter contributions weighted by absorption and internal efficiencies of 70nm and 77nm wide sections:

### S2.6.1. Electro-thermal and geometric parameters

We followed [8] to simulate electrothermal evolution of the hotspot. For the critical current density, sheet resistance, kinetic inductance, we could get the numbers directly, for other electrothermal parameters, we used the values reported in [8] as initial guess and adjusted them to get better fit to the experimental pulses.

#### Geometric parameters

$\bar{d}$ (nm)	$\bar{w}_1$ (nm)	$\bar{w}_2$ (nm)	Length <sub>1</sub> (μm)	Length <sub>2</sub> (μm)	Area <sub>1</sub> (μm <sup>2</sup> )	Area <sub>2</sub> (μm <sup>2</sup> )
8.5	70	77	60.7	465	4.25	35.86

$d$  = film thickness of the tested sample.  $w_1$  &  $w_2$  denote the nanowire width in the two section.

Area 1 = area covered by the narrower section ( $w_1 = 70$  nm)

Area 2 = area covered by the wider section ( $w_2 = 77$  nm)

## Electrothermal parameters

$j_{c0}$ (nA/nm <sup>2</sup> )	$\rho_{10\text{ K}}$ ( $\mu\Omega\cdot\text{cm}$ )	$L_k$ (nH)	$\alpha$ (W/m <sup>2</sup> K)	$c_N$	$c_S$	$\kappa_N$	$\kappa_S$	$T_{\text{sub}}$ (K)	$T_c$ (K)	$C_{\text{bt}}$ (nF)
85	427	448	$5.5 \times 10^5$	$2c_N^*$	$\frac{c_S^*}{4}$	$\frac{\kappa_N^*}{2}$	$2\kappa_S^*$	2.8	10.5	20

\* in the table denotes the values reported in [8]. Here  $j_{c0}$  denotes the critical current density at zero temperature ( $T = 0\text{ K}$ ).  $\rho_{10\text{ K}}$  is the sheet resistance at  $T = 10\text{ K}$ .  $c_N$ ,  $c_S$ ,  $\kappa_N$ ,  $\kappa_S$  represent thermal boundary conductivity, specific heat in superconducting state, specific heat in normal state, normal state thermal conductivity, and superconducting state thermal conductivity, respectively.

The measured switching current was  $I_{\text{sw}} = 38.9\text{ }\mu\text{A}$  at  $T = 2.8\text{ K}$ , which was limited by the 70-nm part of the hybrid SNSPD. Therefore, the switching current density at  $T = 2.8\text{ K}$  was  $j_c = \frac{I_{\text{sw}}}{w_{\text{min}} d_{\text{min}}} = 73.4\text{ nA/nm}^2$ . The switching current density at  $T = 0$ ,  $j_{c0}$  was calculated by:  $j_{c0} = \frac{j_c}{\left(1 - \left(\frac{T}{T_c}\right)^2\right)^2}$ ,

and  $j_c$  at other temperature was calculated using:  $j_c = j_{c0} \cdot \left(1 - \left(\frac{T}{T_c}\right)^2\right)^2$ .

Our adjustment of parameters includes:  $a = 5.5\text{E}5\text{ W/m}^2\text{K}$ ,  $c_N = 2c_N^*$ ,  $c_S = c_S^*/4$ ,  $\kappa_N = \kappa_N^*/2$ ,  $\kappa_S = 2\kappa_S^*$ . The slew rate of the simulated pulse at (6.5 V/ns) was close to that of experimental pulse (6.76 V/ns), Fig. S 9, and this was achieved by considering the Gain of the amplifier to be 64.5 dB (slightly higher than measured ~62dB). The Gain spectrum of the amplifier was not considered in this simulation.

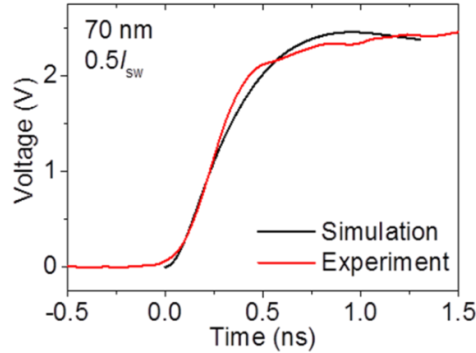


**Fig. S 9, The fit to a detection pulse of the detector was used to adjust eletrothermal simulation parameters.**

We used the noise level at the output of the amplifier, as shown in Fig. S 10, and calculated back the input referred noise (dividing by gain of the amplifier). The input noise level was used to calculate the electronic noise induced jitter,

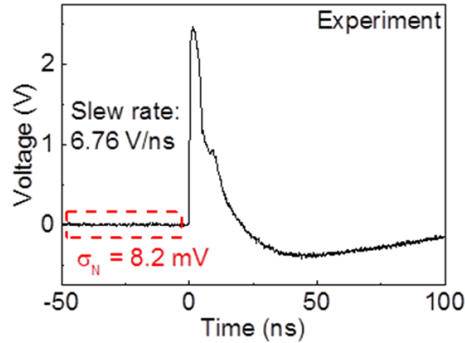


**Fig. S 10, We calculated input referred noise from the output pulse noise level ( $\sigma_N$ ) and the gain of the amplifier.**

The electronic noise induced jitter was then simulated by considering a Gaussian distribution function for voltage noise:

$$\text{Noise is Gaussian function: } e^{-\frac{(V-\bar{V})^2}{2\sigma_N^2}}$$

The slew rate depends on the bias and the nanowire width. Therefore for each section of the nanowire and for each bias current we can calculate an “effective time delay”:  $T_{J_{noise}} = \frac{\sigma_N}{\text{Slew rate}}$

The results are shown in Fig. S 11.

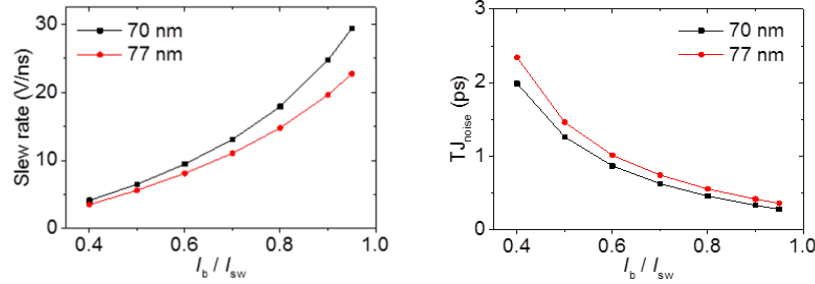


Fig. S 11, Simulated slew rate and time delay for the two sections of the nanowire.

The deviation of these values from experimental observation could have been caused by an imperfect fit to the experimental pulses.

### S2.6.2. The transmission line effect

The detection events taking place in different parts of the nanowire would experience a different transmission line length to the readout output. The amount of such delay depends on the kinetic inductance of nanowire sections and the capacitance between nanowire sections and the ground. For consistency, here we follow literature in calculating the transmission line effect (despite our experimental observation about the low timing jitter suggesting possible different mechanisms for the propagation of detection pulses). Fig. S 12 shows our model to calculate the transmission line delay. Note that, since the thickness of Si is ~1000 times larger than the thickness of  $\text{SiO}_2$  (which is between the NbTiN layer and Silicon in real devices),  $\text{SiO}_2$  was excluded from the capacitance calculation.

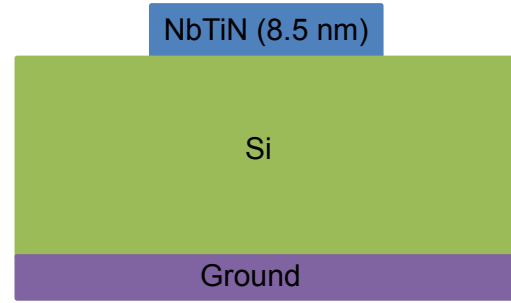


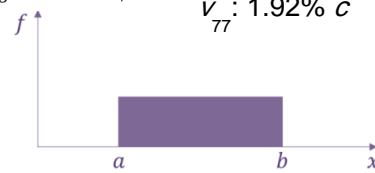
Fig. S 12, Our model for calculating transmission line effect.

Using AppCAD™ to calculate the capacitance per length, we get:  $C_{g\ 70}$ : 35.32 pF/m, and  $C_{g\ 77}$ : 35.65 pF/m and Kinetic inductance per length was calculated from the pulse decay to be:  $L_{g\ 70}$ : 0.93 nH/□m,  $L_{g\ 77}$ : 0.84 nH/□m. This gives:

$$\text{RF signal velocity: } v = \frac{1}{\sqrt{C_g \cdot L_g}} \rightarrow \begin{aligned} v_{70} &: 1.84\% c \\ v_{77} &: 1.92\% c \end{aligned}$$

flood illumination →

The time delay along the nanowire is a uniform distribution:



$$\text{Probability density function: } f = \frac{1}{b-a} \quad \text{Mean: } E(x) = \int_a^b x \cdot f(x) dx = \frac{1}{b-a} \int_a^b x dx = \frac{a+b}{2}$$

$$\text{Standard deviation: } Std = \sqrt{\int_a^b [x - E(x)]^2 \cdot f(x) dx} = \sqrt{\frac{1}{b-a} \int_a^b \left(x - \frac{a+b}{2}\right)^2 dx} = \frac{b-a}{2\sqrt{3}}$$

However, this does not match our experimental observation Fig. S 14. A Gaussian distribution match our experimental results better.

### S2.6.3. The effect of inhomogeneity

The probability density of  $w$ ,  $d$  and  $\Delta$  along the nanowire are considered to be Gaussian functions:

$$e^{-\frac{(w-\bar{w})^2}{2\sigma_w^2}}, e^{-\frac{(d-\bar{d})^2}{2\sigma_d^2}}, \text{ and } e^{-\frac{(\Delta-\bar{\Delta})^2}{2\sigma_{\Delta}^2}}.$$

$\sigma_w/\bar{w}$	$\sigma_d/\bar{d}$	$\sigma_{\Delta}/\bar{\Delta}$	$I_g^w$ (nm)	$I_g^d$ (nm)	$I_g^{\Delta}$ (nm)
1%	2%	5%	5	5	50

We use the function  $f = a \cdot \exp[-\frac{1}{2}(\frac{t-t_1}{TJ_{inhomogeneity}})^2]$  to fit the histograms from electro-thermal simulation, the fitting parameters are listed in the following table: (the inflection at  $0.3I_{sw}$  is due to the use of Gaussian functions to fit the simulated histogram with exponential tail)

$I_b / I_{sw}$	70 nm			77 nm		
	$a$	$t_1$	$TJ_{inhomogeneity}$	$a$	$t_1$	$TJ_{inhomogeneity}$
0.4	0.1101	325.4	8.39336	0.1157	365.7	9.56715
0.5	0.08501	274.4	7.55897	0.09649	309.9	8.18123
0.6	0.0833	237.3	6.1391	0.07957	270.5	7.2832
0.7	0.0898	205.7	4.67256	0.08936	238.5	5.66958
0.8	0.08312	176.4	3.70524	0.08543	209.5	4.4873
0.9	0.09	147.7	3.06248	0.08506	182	3.70948
0.95	0.09381	132.9	2.65377	0.08978	168.3	3.38633

### S2.6.4. The effect of internal efficiency

The contribution of each of 70nm and 77nm wide sections to the overall jitter is determined by both the active area of each section and its relative internal efficiency.

The relative total detection efficiency determines the area under curve for each peak in the overall jitter histogram. Therefore, a good estimation for the internal efficiency of each section is required to match the experimental data. Fig. S 13 shows internal efficiency (measured and fitted) for a test sample and the relative total efficiency curves (calculated by also taking into account the absorption for different sections) used in our simulations .

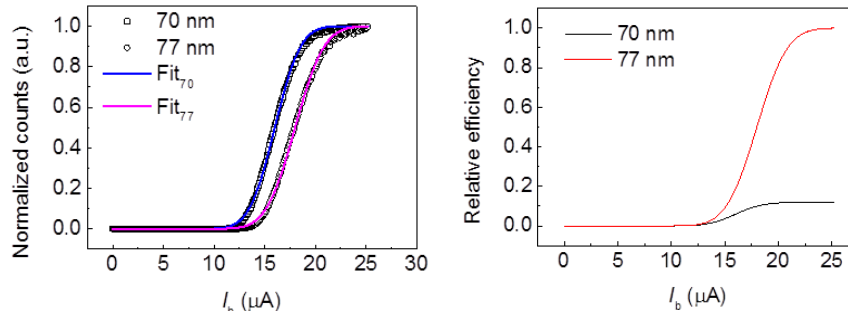
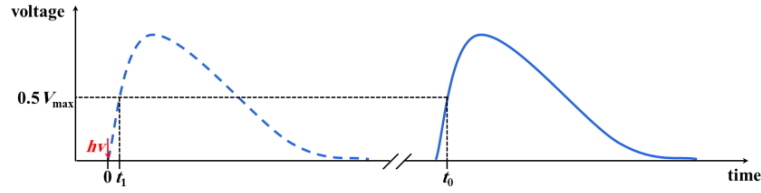


Fig. S 13, Internal efficiency (measured and fitted) and relative total efficiency curves (calculated by taking into account the absorption for different sections) for a test sample.

### S2.6.5. The overall jitter

The overall time delay is calculated from the rising edge of the signal (electro-thermal evolution) and the transmission line effect:





$0 \rightarrow t_1$ : electro-thermal evolution

$t_1 \rightarrow t_0$ : transmission line effect,  $Dt$

$0 \rightarrow t_0$ : overall time delay

$$t_0 = t_1 + \Delta t$$

Similarly the overall time jitter can be calculated as following:

$$TJ_{\text{overall}} = \sqrt{TJ_{\text{noise}}^2 + TJ_{\text{geometric}}^2 + TJ_{\text{inhomogeneity}}^2}$$

For each bias current, we can get two functions for 70nm wide and 77nm wide sections, Each function has such form:

$$F = A_0 \cdot \exp\left[-\frac{1}{2} \left(\frac{t - t_0}{TJ_{\text{overall}}}\right)^2\right]$$

$A_0$  is determined by the relative efficiency between 70 and 77:  $\frac{\int F_{70} dx}{\int F_{77} dx} = \frac{DE_{70}}{DE_{77}}$ .

the overall histograms are given by:  $F_{70} + F_{77}$ . Finally, by considering all contributions we end up in the final simulation results as shown in the Fig. S 14. One can observe that the results by excluding transmission line effect is closer to our experimental observations (see the main text).

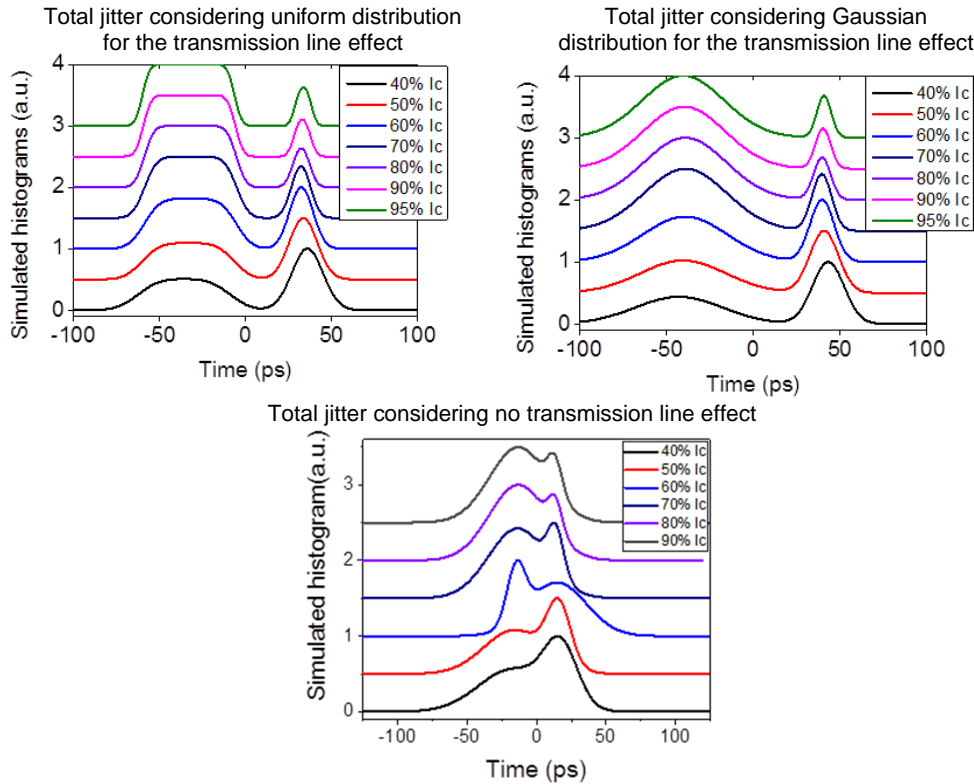


**Fig. S 14, Total jitter considering uniform and Gaussian distribution for the transmission line effect. The latter provides a better agreement with our experimental observations. The closest match can be made when not including the transmission line effect at all.**

## S3- Multi-pixel SNSPDs

### S3.1. RF crosstalk and device performance at different wavelength

RF crosstalk between the pixels is a major concern. If the signal routings are next to one another with no grounding in between, a significant crosstalk is observed, as shown in Fig. S 15(a), while adding the ground lines in between (at least  $\sim 3\times$  thicker than nanowire width) ensures a crosstalk-free performance, Fig. S 15(b).

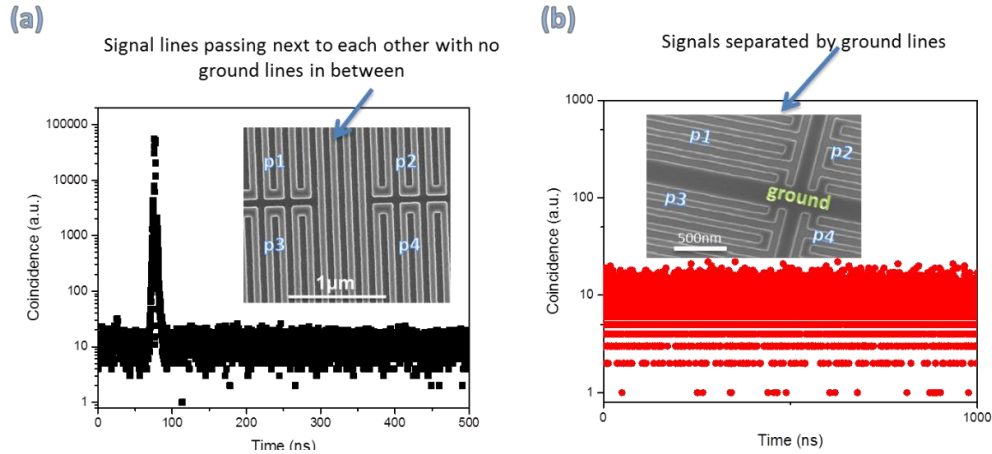


**Fig. S 15, Cross talk measurement for two devices: (a) without grounding between signal lines, exhibiting a high level of crosstalk, and (b) with grounding between pixels with no noticeable crosstalk.**

### S3.2. 16-pixel SNSPD performance at different wavelength

We measured our 16-pixel device at other wavelength that is mentioned in the main text (660nm). The performance is similar, however, due to the multimode illumination (an SMF28 fiber placed far from the sample was used to illuminate the sample), some pixels get slightly higher photon flux than the other ones depending on the wavelength and the excited modes at the launch.

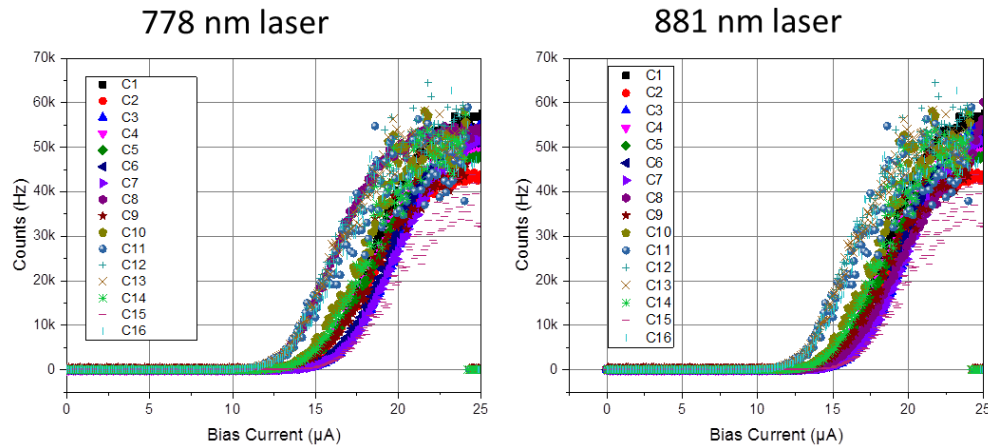


**Fig. S 16, photon count rate measurement for the 16-pixel device at two wavelengths of 778nm and 881 nm.**

### S3.3. Photon antibunching with multi-pixel detectors

As discussed in the main text, we performed antibunching measurement on a nanowire quantum dot. The emission spectrum of the quantum dot and the unprocessed antibunching data (for the same pairs of detectors as discussed in the main text) are shown in Fig. S 17 (a) and (b) respectively.



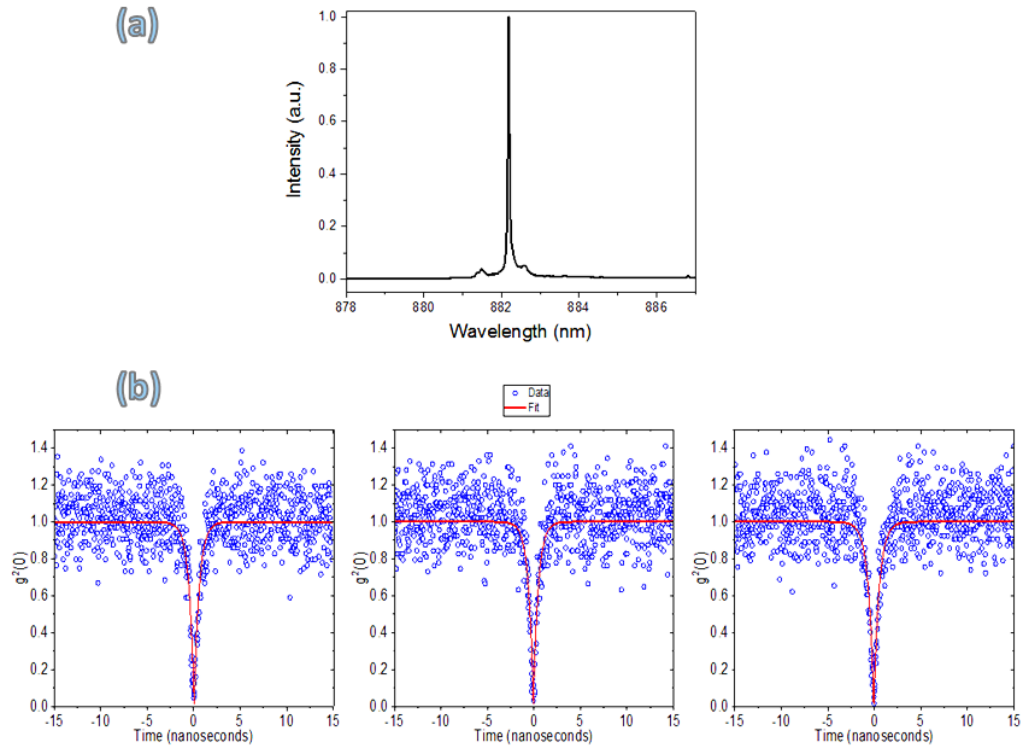


**Fig. S 17, (a) Emission spectrum of nanowire quantum dot used in the antibunching experiment. (b) unprocessed data of correlation measurements for the same pairs as the main text.**

It was mentioned in the main text that the overall time jitter of the experiment was limited by the time dispersion of spectrometer. We used an 1800 grooves per mm grating, kept the input slit of the spectrometer fixed at 50 $\mu$ m and varied the size of output slit. Below are our experimental observations for different output slit sizes:

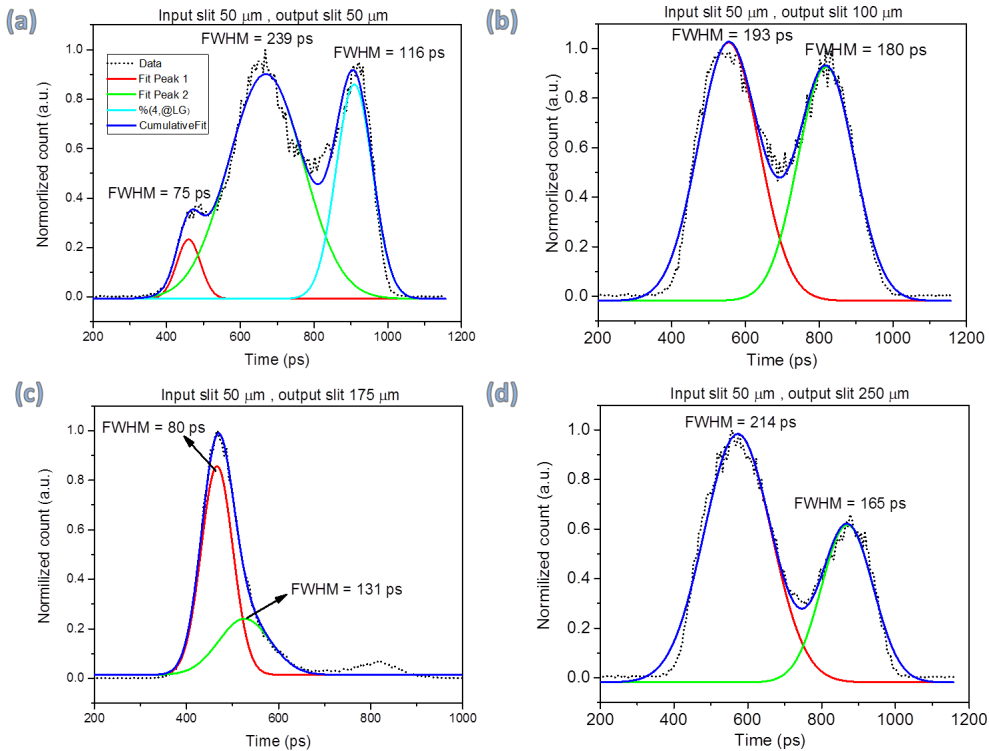


**Fig. S 18, spectrometer time dispersion a function of monochromator output slit size.**

The direct time jitter measurement on the detector yielded ~60ps time resolution (no cryoamp was used) both using a single mode and multimode fiber coupling.

## Bibliography

- [1] I. E. Zadeh, J. W. N. Los, R. B. M. Gourgues, V. Steinmetz, G. Bulgarini, S. M. Dobrovolskiy, V. Zwiller and S. N. Dorenbos, "Single-photon detectors combining high efficiency, high detection rates, and ultra-high timing resolution," *APL Photonics*, vol. 2, no. 11, 2017.
- [2] M. Sidorova, A. Semenov, H.-W. Hübers, I. Charaev, A. Kuzmin, S. Doerner and M. Siegel, "Physical mechanisms of timing jitter in photon detection by current-carrying superconducting nanowires," *Phys. Rev. B*, vol. 96, no. 18, 2017.
- [3] Q. Zhao, L. Zhang, T. Jia, L. Kang, W. Xu, J. Chen and P. Wu, "Intrinsic timing jitter of superconducting nanowire single-photon detectors," *Applied Physics B*, vol. 104, no. 3, pp. 673-678, 2011.
- [4] L. You, X. Yang, Y. He, W. Zhang, D. Liu, W. Zhang, L. Zhang, L. Zhang, X. Liu, S. Chen, Z. Wang and X. Xie, "Jitter analysis of a superconducting nanowire single photon detector," *AIP Advances*, vol. 3, no. 7, p. 072135, 2013.
- [5] N. Calandri, Q.-Y. Zhao, D. Zhu, A. Dane and K. K. Berggren, "Superconducting nanowire detector jitter limited by detector geometry," *Applied Physics Letters*, vol. 109, no. 15, p. 152601, 2016.
- [6] Y. Cheng, C. Gu and X. Hu, "Inhomogeneity-induced timing jitter of superconducting nanowire single-photon detectors," *Applied Physics Letters*, vol. 111, no. 6, p. 062604, 2017.
- [7] J. K. W. Yang, A. J. Kerman, E. A. Dauler, V. Anant, K. M. Rosfjord and K. K. Berggren, "Modeling the Electrical and Thermal Response of Superconducting Nanowire Single-Photon Detectors," *IEEE Transactions on Applied Superconductivity*, vol. 17, no. 2, pp. 581-585, 2007.
- [8] J. Chang, I. E. Zadeh, J. W. N. Los, J. Zichi, A. Fognini, M. Gevers, S. Dorenbos, S. F. Pereira, P. Urbach and V. Zwiller, "Multimode-fiber-coupled superconducting nanowire single-photon detectors with high detection efficiency and time resolution," *Applied Optics*, vol. 58, no. 36, pp. 9803-9807, 2019.